J. Fluid Mech. (1997), *vol.* 340, *pp.* 83–100. Printed in the United Kingdom

Chaotic rotation of triaxial ellipsoids in simple shear flow

By A. L. YARIN, O. GOTTLIEB AND I. V. ROISMAN
Faculty of Mechanical Engineering, Technion – Israel Institute of Technology, Haifa 32000, Israel

(Received 19 June 1996 and in revised form 7 November 1996)

Chaotic behaviour is found for sufficiently long triaxial ellipsoidal non-Brownian particles immersed in steady simple shear flow of a Newtonian fluid in an inertialess approximation. The result is first determined via numerical simulations. An analytic theory explaining the onset of chaotic rotation is then proposed. The chaotic rotation coexists with periodic and quasi-periodic motions. Quasi-periodic motions are depicted by regular closed loops and islands in the system Poincaré map, whereas chaotic rotations form a stochastic layer.

1. Introduction

More than 70 years ago Jeffery (1922) calculated the moment of force acting on an arbitrary ellipsoidal particle immersed in creeping shear flow. For the particular case of a spheroidal inertialess particle he deduced that the motion of the particle in a simple shear flow is periodic. Based on Jeffery's result for the moment of force, Gierszewski & Chaffey (1978) gave several numerical examples of the dynamic behaviour of a triaxial ellipsoidal inertialess particle in a simple shear flow. Hinch & Leal (1979) considered the same problem in much more detail and showed that the motion of a triaxial ellipsoid with comparable axes is doubly periodic. They also showed double periodicity for a nearly spheroidal ellipsoid with an arbitrary axis ratio. Some of their results are revised in the present work.

Szeri, Milliken & Leal (1992) and Szeri (1993) studied the rotation of axisymmetric spheroidal particles in two-dimensional recirculating flows (e.g. in a four-roll mill), which are time periodic in a Lagrangian sense from the particles' point of view. They showed that in some cases non-periodic rotation of an axisymmetric particle sets in due to the time-dependent character of flow. In three-dimensional flows the rotation of axisymmetric particles becomes quasi-periodic (Szeri & Leal 1993; Szeri 1993).

The aim of this work is to study the dynamics of a general triaxial ellipsoidal particle with one axis significantly longer than two others. The particle is immersed in a simple shear flow, and inertial effects are neglected for both particle and fluid. The flow is steady in both the Eulerian and Lagrangian (associated with the particle) sense. Nevertheless, it is shown that chaotic rotation of the particle sets in under appropriate conditions due to its non-axisymmetric shape.

In §2 the governing equations and some of the relevant periodic motions of triaxial ellipsoidal particles are outlined. In §3 the stability of the periodic motions is considered via Floquet theory. Chaotic numerical solutions are presented in §4. The analytic theory explaining formation of the stochastic layer is presented and discussed in §5. Conclusions are summarized in §6.

2. Governing equations and relevant periodic motions

Consider a creeping simple shear flow in the plane y', z' (see figure 1) and a small triaxial ellipsoidal particle immersed in it. The particle is assumed to be small enough to neglect inertial effects. The frame of reference x, y, z is 'frozen' in the particle along its axes. The particle's orientation (or x, y, z-axes) relative to the laboratory frame of reference x', y', z' is, as usual, described in terms of the Euler angles ϕ, ψ, θ (figure 1). The laboratory frame of reference x', y', z' may be transformed to that of the particle x, y, z by three rotations: the first around Ox' by ϕ, the second around OK by θ, the third around Ox by ψ (see figure 1). The flow is directed along the z'-axis, with shear along the y'-axis.

The moment of force acting on an inertialess particle and the equations describing its reorientation under the effect of the flow were obtained by Jeffery (1922) (his equations (41)). In the present work these equations take the following form:

$$\frac{\mathrm{d}\theta}{\mathrm{d}t} = (g_2 \sin\psi + g_3 \cos\psi)\sin\theta, \tag{2.1a}$$

$$\frac{\mathrm{d}\phi}{\mathrm{d}t} = \tfrac{1}{2} + g_3 \sin\psi - g_2 \cos\psi, \tag{2.1b}$$

$$\frac{\mathrm{d}\psi}{\mathrm{d}t} = g_1 + (g_2 \cos\psi - g_3 \sin\psi)\cos\theta, \tag{2.1c}$$

where time t is rendered dimensionless by the reciprocal shear rate κ, and the functions g_i are given by the following formulae:

$$g_1 = \frac{a_y^2 - a_z^2}{2(a_y^2 + a_z^2)}[-\tfrac{1}{2}(\cos^2\theta + 1)\sin 2\phi \sin 2\psi + \cos\theta \cos 2\phi \cos 2\psi], \tag{2.2a}$$

$$g_2 = \frac{a_z^2 - a_x^2}{2(a_x^2 + a_z^2)}(-\cos\theta \sin 2\phi \sin\psi + \cos 2\phi \cos\psi), \tag{2.2b}$$

$$g_3 = \frac{a_x^2 - a_y^2}{2(a_x^2 + a_y^2)}(\cos\theta \sin 2\phi \cos\psi + \cos 2\phi \sin\psi). \tag{2.2c}$$

In (2.2) a_x, a_y and a_z correspond to semi-axes of the ellipsoidal particle in the x-, y- and z-directions, respectively.

Equations (2.1) are solved subject to the following initial conditions:

$$t = 0: \quad \theta = \theta_0, \quad \phi = \phi_0, \quad \psi = \psi_0, \tag{2.3a–c}$$

where index zero corresponds to given initial values of the Euler angles.

Equations (2.1) and (2.2) were solved by Jeffery (1922) analytically for a spheroidal particle (with $a_x \neq a_y = a_z$), or for the simplest spherical particle ($a_x = a_y = a_z$), and the solution was shown to lead to periodic motions:

$$\tan\phi = \frac{a_x}{a_z}\tan\left(\frac{a_x a_z}{a_x^2 + a_z^2}t\right), \quad \tan\theta = C a_x (a_x^2 \cos^2\phi + a_z^2 \sin^2\phi)^{-1/2}, \tag{2.4a, b}$$

where C is the orbit constant ranging between $-\infty$ and $+\infty$.

Equations (2.1) and (2.2) also possess several simple solutions, which correspond to the rotation of a triaxial ellipsoidal particle about one of its axes x, y or z (simple periodic motions). The axis of rotation x, or y or z coincides with the x'-axis of the laboratory frame of reference.

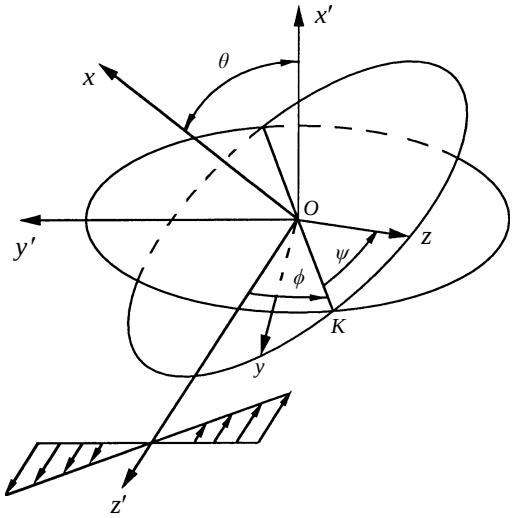

FIGURE 1. Sketch of the frames of reference: immovable x', y', z', and 'frozen' into a particle x, y, z, as well as the Euler angles ϕ, θ, ψ. The velocity profile is also shown.

The solution

$$\phi = \arctan\left[\frac{a_x}{a_y}\tan\left(\frac{a_x a_y}{a_x^2 + a_y^2}\,t\right)\right], \tag{2.5a}$$

$$\theta \equiv \tfrac{1}{2}\pi, \quad \psi \equiv \tfrac{1}{2}\pi + \pi n, \quad n = 0, \pm 1, \pm 2, \ldots, \tag{2.5b, c}$$

$$T = \frac{\pi(a_x^2 + a_y^2)}{a_x a_y} \tag{2.5d}$$

(T is the period of the corresponding motion) describes the case when the z-axis of the particle coincides with x' (figure 2*a*).

The second solution corresponds to the case when the y-axis of the particle coincides with x' (figure 2*b*). This motion is identical to (2.5) with a_x, a_y and a_z replaced by a_z, a_x and a_y, respectively. The angle θ in this case is defined in figure 2(*b*); it is different from that of figure 1.

If in (2.5) we replace a_x, a_y and a_z by a_y, a_z and a_x, respectively, and redefine angle θ, as shown in figure 2(*c*), we obtain the solution corresponding to particle rotation about its x-axis which coincides with the fixed x'-axis.

3. Stability of periodic motions

The stability of periodic motions of the particle corresponding to solutions (2.5) has been studied using Floquet theory (e.g. Joseph 1976). Denote the solution vector by $\boldsymbol{X} = [\theta, \phi, \psi]$ and express the set of differential equations (2.1) in the form

$$\dot{\boldsymbol{X}} = \boldsymbol{F}(\boldsymbol{X}). \tag{3.1}$$

Periodic motions correspond to $\boldsymbol{X} = \boldsymbol{X}_{per}$. Let these periodic motions be perturbed by small perturbation $\boldsymbol{Y}$, and then $\boldsymbol{X} = \boldsymbol{X}_{per} + \boldsymbol{Y}$. Linearizing (3.1) and accounting for the fact that $\boldsymbol{X}_{per}$ satisfies (3.1), we arrive at

$$\dot{\boldsymbol{Y}} = \boldsymbol{A}(t)\cdot\boldsymbol{Y}, \quad \boldsymbol{A} = \partial\boldsymbol{F}/\partial\boldsymbol{X}|_{\boldsymbol{X}_{per}}. \tag{3.2a, b}$$

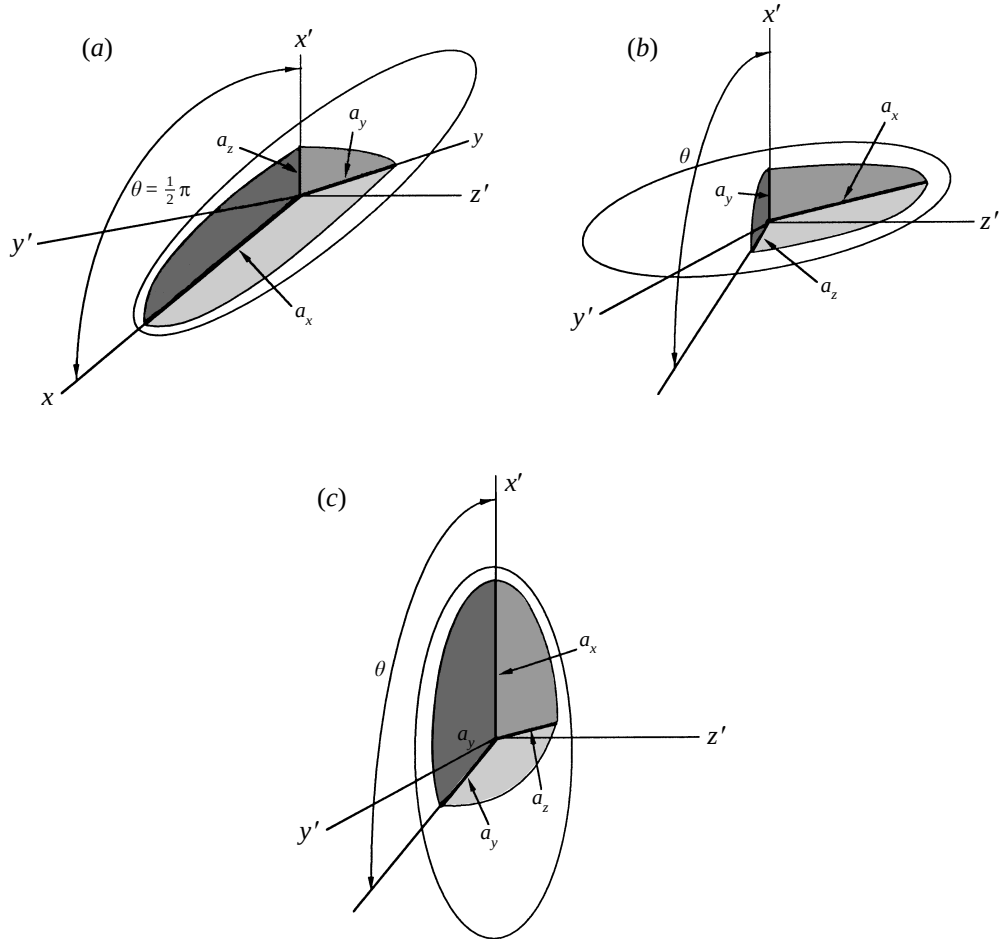

FIGURE 2. Triaxial ellipsoid rotating about (*a*) the *z*-axis ($x' \equiv z$), (*b*) the *y*-axis ($x' \equiv y$), and (*c*) the *x*-axis ($x' \equiv x$).

The equations describing the perturbations $\boldsymbol{Y} = [\delta\theta, \delta\phi, \delta\psi]$ of the solution (2.5) are obtained with the help of (2.1) and (3.2*b*) as

$$\delta\dot{\theta} = A_{11}(t)\,\delta\theta + A_{13}(t)\,\delta\psi, \quad \delta\dot{\phi} = A_{22}(t)\,\delta\phi, \quad \delta\dot{\psi} = A_{31}(t)\,\delta\theta + A_{33}(t)\,\delta\psi, \tag{3.3.a–c}$$

where

$$A_{11}(t) = \frac{a_z^2 - a_x^2}{2(a_x^2 + a_z^2)}\sin(2\phi_{per}), \quad A_{13}(t) = \frac{(a_y^2 - a_z^2)\,a_x^2}{(a_x^2 + a_y^2)(a_x^2 + a_z^2)}\cos(2\phi_{per}), \tag{3.4a, b}$$

$$A_{22}(t) = \frac{a_y^2 - a_x^2}{(a_y^2 + a_x^2)}\sin(2\phi_{per}), \quad A_{31}(t) = \frac{(a_x^2 - a_z^2)\,a_y^2}{(a_x^2 + a_y^2)(a_y^2 + a_z^2)}\cos(2\phi_{per}), \tag{3.4c, d}$$

$$A_{33}(t) = \frac{a_y^2 - a_z^2}{2(a_y^2 + a_z^2)}\sin(2\phi_{per}), \quad \phi_{per} = \arctan\left[\frac{a_x}{a_y}\tan\left(\frac{a_x a_y}{a_x^2 + a_y^2}\,t\right)\right]. \tag{3.4e, f}$$

Note that (3.3*b*) is decoupled from (3.3*a*, *c*) yielding via (3.4*c*, *f*) a periodic solution for $\delta\phi$. Consequently, the stability of (2.5) reduces to the analysis of equations (3.3*a*) and (3.3*c*).

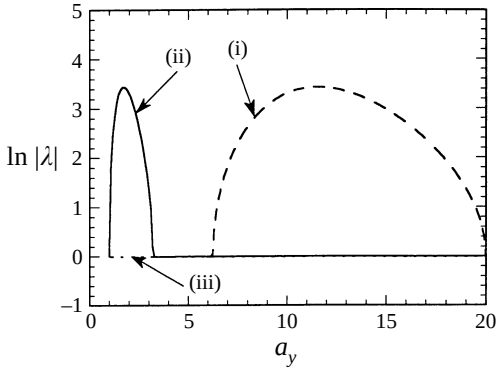

FIGURE 3. Floquet multiplier for a long triaxial ellipsoid with $a_x = 20$, $a_z = 1$, and $1 < a_y < 20$: (i) $x' \equiv x$; (ii) $x' \equiv z$; (iii) $x' \equiv y$.

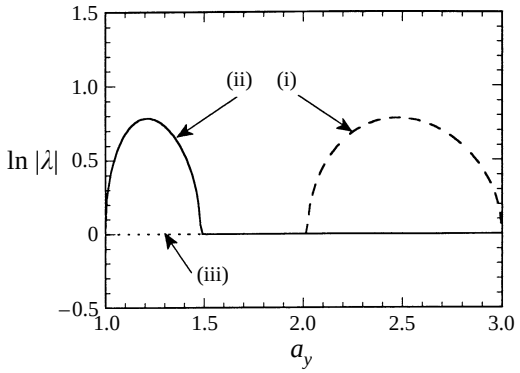

FIGURE 4. Floquet multiplier for a short triaxial ellipsoidal particle with $a_x = 3$, $a_z = 1$, and $1 < a_y < 3$: (i) $x' \equiv x$; (ii) $x' \equiv z$; (iii) $x' \equiv y$.

The monodromy matrix $\boldsymbol{C} = \boldsymbol{\Phi}(t = T)$ is obtained by means of numerical solution of the problem:

$$\dot{\boldsymbol{\Phi}} = \begin{bmatrix} A_{11}(t) & A_{13}(t) \\ A_{31}(t) & A_{33}(t) \end{bmatrix} \cdot \boldsymbol{\Phi}, \tag{3.5}$$

subject to the initial condition

$$\boldsymbol{\Phi}(t = 0) = \boldsymbol{I}, \tag{3.6}$$

where $\boldsymbol{I}$ is the unit tensor.

The same procedure is applicable to the cases depicted in figure 2(*b*, *c*).

In order to check stability of periodic motions of a triaxial ellipsoidal particle, consider the Floquet multipliers λ_1, λ_2, which are the eigenvalues of the monodromy matrix $\boldsymbol{C}$. According to Floquet theory, for $\ln|\lambda| > 0$ the motion is unstable and for $\ln|\lambda| < 0$ it is stable.

The results of the computations of $\ln|\lambda|$ for the three above-mentioned solutions corresponding to (2.5) (figure 2*a–c*) with $a_x = 20$ and $a_z = 1$ are shown in figure 3 for a_y in the range $a_z \leqslant a_y \leqslant a_x$. The motion corresponding to the case $z \equiv x'$ loses its stability at $1 < a_y < 3.20$, whereas for higher values of a_y it is stable. The motion corresponding to the case $y \equiv x'$ is neutrally stable in the whole range $1 \leqslant a_y \leqslant 20$. The motion corresponding to the case $x \equiv x'$ loses its stability for $6.26 < a_y < 20$, whereas it is stable for smaller values of a_y. The corresponding graphs for a much shorter particle ($a_x = 3$, $a_z = 1$), are shown in figure 4. For this particle the motion

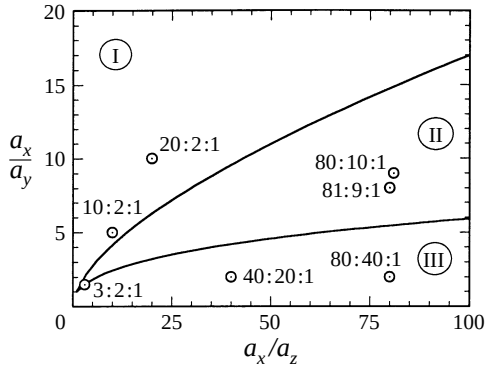

FIGURE 5. Stability map. In domain I the periodic motion $z \equiv x'$ is unstable, whereas $y \equiv x'$ and $x \equiv x'$ are stable. In domain II $z \equiv x'$, $y \equiv x'$ and $x \equiv x'$ are stable. In domain III $x \equiv x'$ is unstable, whereas $z \equiv x'$ and $y \equiv x'$ are stable. Some points corresponding to the particles studied in more detail in the present paper are also shown – they are marked by their $a_x : a_y : a_z$ ratio.

corresponding to the case $z \equiv x'$ is unstable in the range $1 < a_y < 1.48$; the motion corresponding to the case $y \equiv x'$ is neutrally stable in the whole range $a_z \leqslant a_y \leqslant a_x$; the motion corresponding to the case $x \equiv x'$ is unstable in the range $2.02 < a_y < 3$.

The complete results of the stability analysis are plotted in figure 5. There, in domain I, the periodic motion with $z \equiv x'$ is unstable, whereas the periodic motions $y \equiv x'$ and $x \equiv x'$ are stable. In domain II all the periodic motions ($z \equiv x'$, $y \equiv x'$ and $x \equiv x'$) are stable. In domain III the periodic motion $x \equiv x'$ is unstable, whereas $z \equiv x'$ and $y \equiv x'$ are stable. In figure 5 the points corresponding to some specific particles studied in more detail in the present paper are also shown.

Note that the Floquet theory used in the present work accurately reproduced the stability analysis of the periodic motions obtained by Hinch & Leal (1979) via an alternative method (their table 1).

4. Numerical solution: chaotic behaviour

Equations (2.1) with initial conditions (2.3), which do not correspond to the simple periodic motions discussed in §3, were solved numerically for sufficiently long triaxial ellipsoidal particles. Some details on the numerical integration are discussed in the Appendix. An example particle with $a_x = 20$, $a_y = 2$, and $a_z = 1$ is first considered. From here on, the definition of θ corresponds to that of figure 1. The examples of figure 6(*a*), close to one of the stable periodic solutions found in §3 for this case (y is parallel to x': $\theta = \frac{1}{2}\pi$ with $\psi = 0$) led to quasi-periodic motions manifesting themselves as closed loops on the Poincaré map sampled (following Hinch & Leal 1979) every $\phi = n\pi$. Note that the transition regions between quasi-periodic motions and the aperiodic stochastic layer are characterized by isolated closed-loop islands (solutions 5, 6, 7 and 9 in figure 6*a*).

The whole space outside the area filled by closed loops in the Poincaré map of figure 6(*a*) is populated by chaotically placed dots forming a stochastic layer. This stochastic layer approaches the periodic solution $\theta = \frac{1}{2}\pi$, $\arcsin(\sin(\psi)) = \frac{1}{2}\pi$ corresponding to z parallel to x', which is unstable as determined by Floquet theory in the previous section. However, the stochastic layer does not approach the periodic motions $\theta = 0$ or π corresponding to x parallel to x' (stable as determined by Floquet theory in §3) and is separated from them by regions of quasi-periodic behaviour (e.g. solutions 7, 8, 9 and 10 in figure 6*a*).

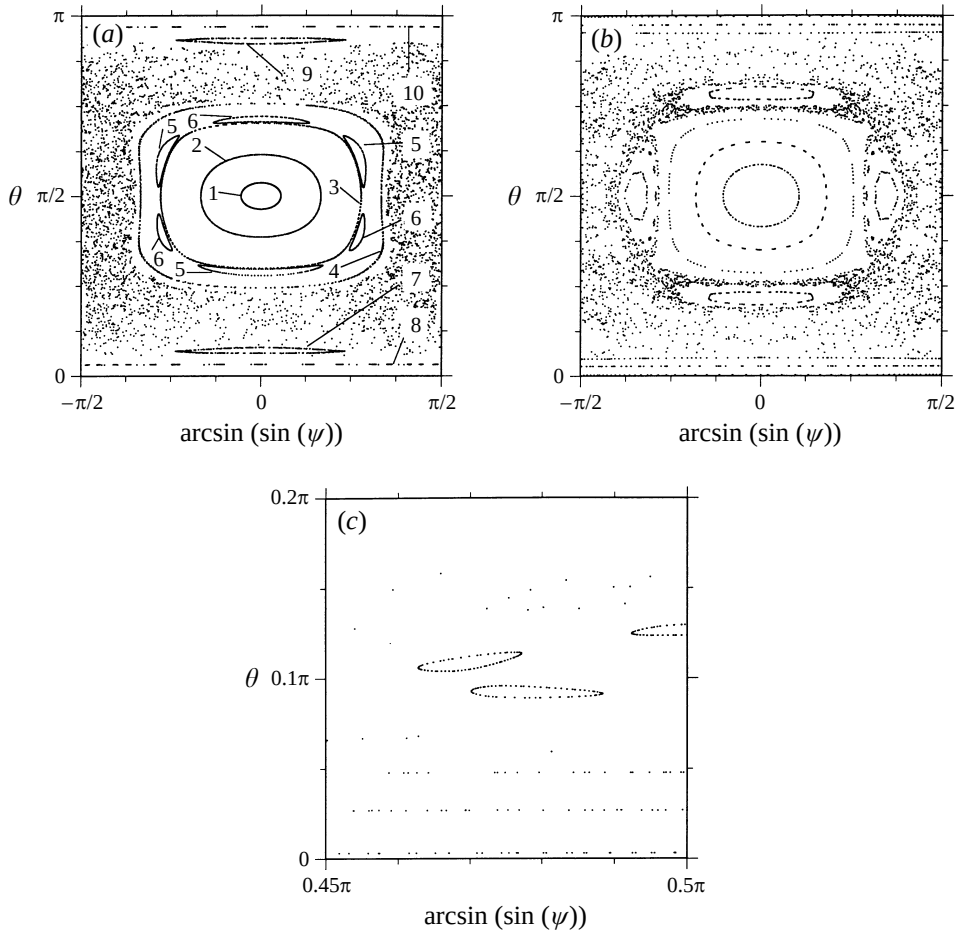

FIGURE 6. (*a*) The Poincaré map ($\theta(\psi)$) for a triaxial ellipsoid with $a_x = 20$, $a_y = 2$, and $a_z = 1$. The dots mark when $\phi = \pi n$. The initial conditions are $\phi_0 = 0$, and 1, $(\theta_0, \psi_0) = (\pi/2, \pi/18)$; 2, $(\pi/2, \pi/6)$; 3, $(\pi/2, 2\pi/9)$; 4, $(\pi/2, \pi/3)$; 5, $(0, 5\pi/18)$; 6, $(65\pi/180, \pi/4)$; 7, $(0.2, 0)$; 8, $(0.1, 0)$; 9, $(\pi-0.2, 0)$; 10, $(\pi-0.1, 0)$. The initial condition leading to the stochastic layer is $\phi_0 = 0$, $\theta_0 = \pi/4$, $\psi_0 = \pi/4$. The axis $\arcsin(\sin(\psi))$ is used instead of ψ to exclude a trivial drift in ψ similar to that described by Hinch & Leal (1979) for the fundamental Jeffery solution (their figure 4), and leading only to the replication of identical physical situations. (*b*) The Poincaré map for a particle with $a_x = 10$, $a_y = 2$, and $a_z = 1$. (*c*) An enlargement of the lower right corner of (*b*) – some quasi-periodic islands are resolved. Rotation with z parallel to x' ($\theta \equiv \pi/2$ and $\psi \equiv \pi/2$) is unstable, whereas rotations with y parallel to x' ($\theta \equiv \pi/2$ and $\psi \equiv 0$) and x parallel to x' ($\theta \equiv 0$ or π) are stable.

A similar Poincaré map corresponding to a particle with $a_x = 10$, $a_y = 2$ and $a_z = 1$ is shown in figure 6(*b*). In the lower right corner of this map (see figure 6*c*) the quasi-periodic islands are also found.

In spite of the fact that the system under consideration is non-Hamiltonian, it is worth recalling that stochastic motion occurs near separatrices separating invariant curves from their islands in near-integrable (Hamiltonian) systems (cf. Lichtenberg & Lieberman 1992).

In figure 7 a section of the time series corresponding to the stochastic layer of figure 6(*a*) is shown. It is clearly seen that angle θ oscillates chaotically about the value of $\frac{1}{2}\pi$. This irregular response has a wide-band spectrum (figure 8*a*) and a positive Lyapunov exponent λ_1 ($\lambda_1 = 0.021$, $\lambda_2 = 0$ and $\lambda_3 = -0.026$) corresponding to a Lyapunov

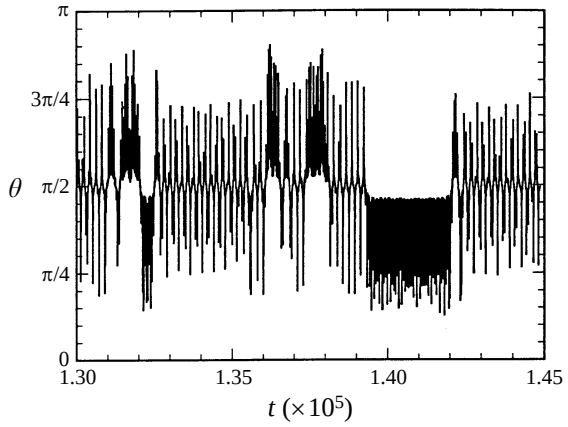

FIGURE 7. Time-series ($\theta(t)$) for a long triaxial ellipsoid with $a_x = 20$, $a_y = 2$, $a_z = 1$, and the initial conditions $\phi_0 = 0$, $\theta_0 = \frac{1}{4}\pi$, and $\psi_0 = \frac{1}{4}\pi$. Chaotic behaviour.

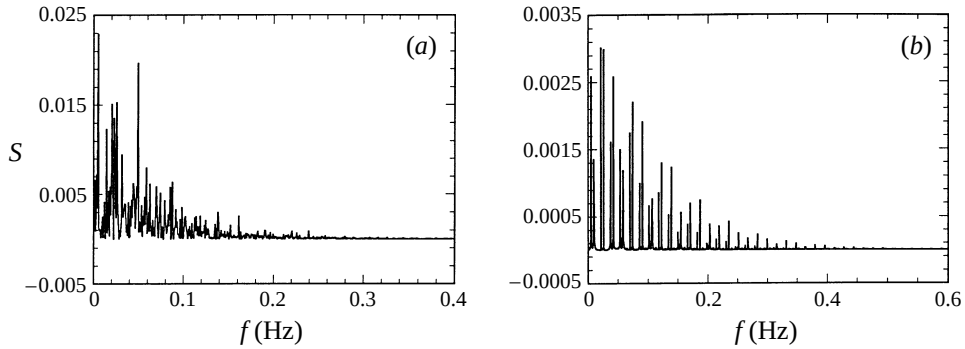

FIGURE 8. (*a*) Spectrum obtained by the fast-Fourier transformation corresponding to the stochastic layer of figure 7. S denotes the spectral power. (*b*) Spectrum corresponding to a quasi-periodic solution (closed loop 2 of figure 6*a*).

dimension of 2.82. In figure 8(*b*) a spectrum corresponding to a quasi-periodic solution (closed loop 2 of figure 6*a*) is also shown for comparison: it clearly consists of a number of delta-functions corresponding to the number of harmonics involved.

The trace of the Jacobian of the present system $\mathrm{Tr}(\boldsymbol{J}) = \partial\dot{\theta}/\partial\theta + \partial\dot{\phi}/\partial\phi + \partial\dot{\psi}/\partial\psi$ oscillates chaotically around zero changing from about -1 to about $+1$ for the stochastic layer of figure 6(*a*). It is emphasized that the trace calculated for the integrable Jeffery-like orbits of §3 is identically zero whereas the numerically calculated trace of both quasi-periodic and chaotic motions does not provide a negative mean value, indicating system attraction.

If one naively prolongs the time series of figure 7 up to much larger values of t, as for example those shown in figure 9, one reaches the almost quasi-periodic behaviour depicted by the Poincaré map of figure 10. Also, irrespective of the numerical method of integration selected, the results can be shown to be time-step-dependent and cannot be reproduced in detail for very long time intervals. The latter observation shows the numerical spuriosity originating from the accumulation of truncation errors leading to a gradual diffusion from the stochastic layer to a central region filled by the quasi-periodic motions in figure 6(*a*). This stresses the idea that chaotic motions are, in principle, uncomputable. However, the chaotic nature of rotation of sufficiently long

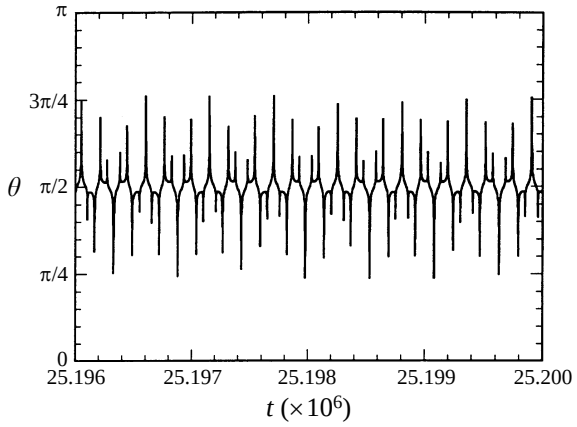

FIGURE 9. The time series corresponding to the conditions of figure 7 prolonged to much higher values of time. Quasi-periodic-like behaviour sets in – a numerical artifact.

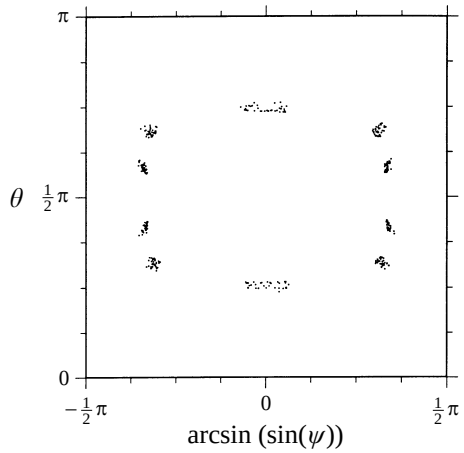

FIGURE 10. The Poincaré map corresponding to the time series of figure 9. The dots mark when $\phi = \pi n$.

triaxial ellipsoidal particles in simple shear flow is explained in §5 via an analytic treatment.

Note also that chaotic motion emerges even for relatively short particles. One of the examples studied in Hinch & Leal (1979) numerically ($a_x = 3$, $a_y = 2$, $a_z = 1$) is re-examined to reveal the formation of a stochastic layer at the corners of the Poincaré map (figure 11). This Poincaré map was plotted with a very fine resolution showing in detail a thin stochastic layer not resolved in figure 5(*b*) of Hinch & Leal (1979). According to §3 this case includes periodic motions with z parallel to x' ($\theta = \frac{1}{2}\pi$, $\psi = \frac{1}{2}\pi$) and with x parallel to x' ($\theta = 0$ or π) that are stable, along with stable periodic motion with y parallel to x' ($\theta = \frac{1}{2}\pi$, $\psi = 0$). Even the fact that the periodic motions are all stable does not preclude formation of the stochastic layer between the regions of the closed-loop 'orbits' in the Poincaré map.

The results of the simulations for much longer particles ($a_x : a_y : a_z = 40:20:1$, $80:40:1$, $80:10:1$ and $81:9:1$) resemble the Poincaré maps shown in figures 6(*a*, *b*) and 11: a central part filled by closed loops corresponding to quasi-periodic motions submerged in a stochastic layer.

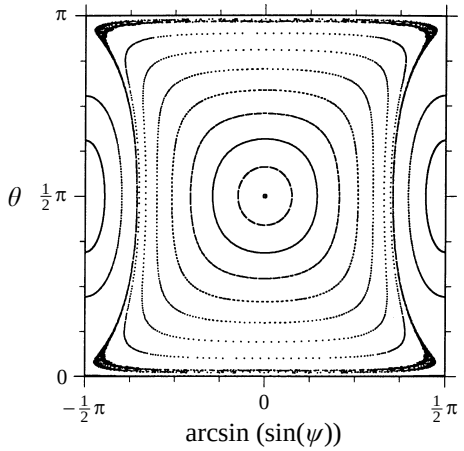

FIGURE 11. The Poincaré map corresponding to a particle with $a_x = 3$, $a_y = 2$ and $a_z = 1$. The dots mark when $\phi = \pi n$. Rotations with x parallel to x' ($\theta \equiv 0$ or π), y parallel to x' ($\theta \equiv \pi/2$ and $\psi \equiv 0$) and z parallel to x' ($\theta \equiv \pi/2$ and $\psi \equiv \pi/2$) are stable.

5. Analytic study of the chaotic motion – slip tunnelling through the plane of shear

To expose the nature of the chaotic motion we consider a very long finite particle assuming

$$a_y^2/a_x^2 = \epsilon A_{yx}^2, \quad A_{yx} = O(1), \tag{5.1 a, b}$$

$$a_z^2/a_x^2 = \epsilon A_{zx}^2, \quad A_{zx} = O(1), \tag{5.1 c, d}$$

where $\epsilon \ll 1$.

We also assume the particle to be a nearly axisymmetric ellipsoid, so that

$$A_{zx}^2 = A_{yx}^2(1 + m\epsilon), \tag{5.2}$$

where m is a negative constant (since we always assume $a_z < a_y$) which is a measure of deviation from axial symmetry; $|m|\,\epsilon$ is considered to be small.

The equations of motion (2.1) with (2.2) under the conditions (5.1) and (5.2) reduce to the following system:

$$\frac{\mathrm{d}\theta}{\mathrm{d}t} = \tfrac{1}{4}\sin 2\theta \sin 2\phi - \tfrac{1}{2}\epsilon A_{yx}^2 \sin 2\theta \sin 2\phi$$
$$+ \epsilon^2 A_{yx}^2[\tfrac{1}{2}A_{yx}^2 \sin 2\theta \sin 2\phi + \tfrac{1}{2}m(-\sin 2\theta \sin 2\phi \sin^2\psi + \cos 2\phi \sin 2\psi \sin\theta)]$$
$$+ O(\epsilon^3), \tag{5.3 a}$$

$$\frac{\mathrm{d}\phi}{\mathrm{d}t} = \cos^2\phi - \epsilon A_{yx}^2 \cos 2\phi$$
$$+ \epsilon^2 A_{yx}^2[A_{yx}^2 \cos 2\phi + m(\tfrac{1}{2}\cos\theta \sin 2\phi \sin 2\psi - \cos 2\phi \cos^2\psi)] + O(\epsilon^3), \tag{5.3 b}$$

$$\frac{\mathrm{d}\psi}{\mathrm{d}t} = -\tfrac{1}{2}\cos\theta \cos 2\phi + \epsilon A_{yx}^2 \cos 2\phi \cos\theta$$
$$+ \tfrac{1}{4}m\epsilon(\tfrac{1}{2}\sin 2\psi \sin 2\phi \cos^2\theta + \tfrac{1}{2}\sin 2\psi \sin 2\phi - \cos\theta \cos 2\phi \cos 2\psi)$$
$$+ \tfrac{1}{8}\epsilon^2 m^2(-\tfrac{1}{2}\sin 2\psi \sin 2\phi \cos^2\theta + \cos 2\psi \cos 2\phi \cos\theta - \tfrac{1}{2}\sin 2\psi \sin 2\phi)$$
$$+ \epsilon^2 A_{yx}^2[m(-\tfrac{1}{2}\cos^2\theta \sin 2\phi \sin 2\psi + \cos\theta \cos 2\phi \cos^2\psi) - A_{yx}^2 \cos\theta \cos 2\phi]$$
$$+ O(\epsilon^3). \tag{5.3 c}$$

Considering terms up to order ϵ in equations (5.3*a*, *b*), one observes that they do not include m, which means that both axisymmetric and nearly axisymmetric particles move along Jeffery's orbits:

$$\tan\phi = a\tan bt, \quad \tan\theta = C(a^2\sin^2 bt + \cos^2 bt)^{1/2}, \tag{5.4a, b}$$

where

$$a = \left[\frac{1-\epsilon A_{yx}^2}{\epsilon A_{yx}^2}\right]^{1/2}, \quad b = A_{yx}[\epsilon(1-\epsilon A_{yx}^2)]^{1/2}. \tag{5.5a, b}$$

Periodic solutions (5.4) are obtained by integration of (5.3*a*, *b*) up to $O(\epsilon)$, or directly as an asymptotic of (2.4).

Note that $a \approx \epsilon^{-1/2}A_{yx}^{-1}$ and $b \approx \epsilon^{1/2}A_{yx}$ as $\epsilon \to 0$ in (5.5).

It is also worth noting that $bt \approx A_{yx}\epsilon^{1/2}t$ which via (5.4) means that traversing Jeffery's orbits by long particles (both axisymmetric and non-axisymmetric) becomes slow on the time scale of t. The latter makes the asymptotic technique employed in §6 of Hinch & Leal (1979) inapplicable to long particles since their fast and slow times merge. Therefore, their result that motion of a nearly axisymmetric ellipsoid is doubly periodic cannot be applied to the long nearly axisymmetric particles which are considered in this section.

Solution (5.4) shows that all Jeffery's orbits with $C = O(1)$ at the time instants $bt = \frac{1}{2}\pi + \pi n$ approach $\theta = \frac{1}{2}\pi$, whereas ϕ approaches $\frac{1}{2}\pi + \pi n$, $n = 0, \pm 1, \pm 2 \ldots$. Angle ψ may at these instants approach any value ψ_* in the range $-\frac{1}{2}\pi < \psi_* < \frac{1}{2}\pi$. When these Jeffery's orbits approach the plane of shear $\theta = \frac{1}{2}\pi$ with $\phi = \frac{1}{2}\pi + \pi n$, the leading-order terms in (5.3) cancel, and in a thin slice near this plane the problem has to be reconsidered separately. To do this, we assume that

$$\theta = \tfrac{1}{2}\pi - \Delta\theta, \quad \phi = \tfrac{1}{2}\pi - \Delta\phi, \quad \psi = \psi_* - \Delta\psi, \tag{5.6a–c}$$

where the increments $\Delta\theta$, $\Delta\phi$ and $\Delta\psi$ are small. The cyclic angle πn is not included for brevity.

If the particle apex approaches sufficiently close to the plane of shear $\theta = \frac{1}{2}\pi$ to allow passage through it (as will be seen below) the following conditions are posed:

$$t = t_*: \quad \Delta\theta = \Delta\psi = 0, \quad \Delta\phi = \Delta\phi_*, \tag{5.7–a–c}$$

where t_* is the instant when passage occurs, and $\Delta\phi_*$ is the value of $\Delta\phi$ at this instant. Considering short time intervals $t - t_* = O(1)$ and substituting (5.6) into (5.3), we arrive at the following equations written to the leading order:

$$\frac{\mathrm{d}\Delta\theta}{\mathrm{d}t} = (-\epsilon^2 A_{yx}^2 m\cos 2\psi_*)\,\Delta\psi + \tfrac{1}{2}\epsilon^2 A_{yx}^2 m\sin 2\psi_*, \tag{5.8a}$$

$$\frac{\mathrm{d}\Delta\psi}{\mathrm{d}t} = -\tfrac{1}{2}\Delta\theta - \tfrac{1}{4}m\epsilon\sin 2\psi_*\,\Delta\phi, \tag{5.8b}$$

$$\frac{\mathrm{d}\Delta\phi}{\mathrm{d}t} = -\Delta\phi^2 - \epsilon A_{yx}^2. \tag{5.8c}$$

Consider the case where ψ_* is different from 0 or $\pm\frac{1}{2}\pi$, which allows the neglect of the first term on the right in (5.8*a*). The solution of (5.8) is then given up to the leading order by

$$\Delta\theta = \tfrac{1}{2}\epsilon^2 A_{yx}^2 m\sin 2\psi_*(t - t_*), \tag{5.9a}$$

$$\Delta\psi = -\tfrac{1}{4}m\epsilon\sin 2\psi_*\,\Delta\phi_*(t - t_*), \tag{5.9b}$$

$$\Delta\phi \simeq \Delta\phi_* - \epsilon A_{yx}^2(t - t_*). \tag{5.9c}$$

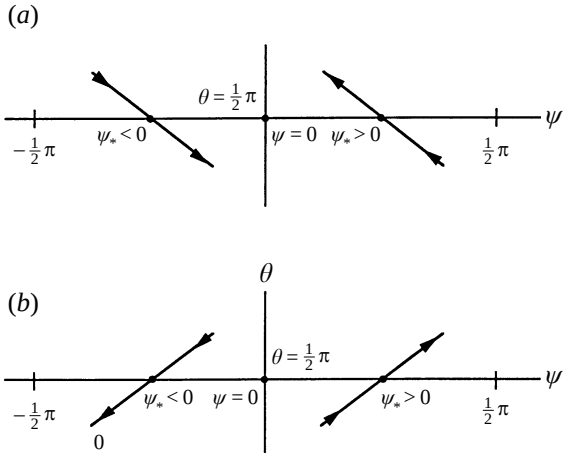

FIGURE 12. The orbits of a non-axisymmetric particle on the phase plane θ, ψ, when it passes through the plane $\theta = \frac{1}{2}\pi$. Note that only points corresponding to $\phi = \pi n$ separated from the orbits enter Poincaré maps of the type of figures 6 and 11. (*a*) $\Delta\phi_* > 0$, (*b*) $\Delta\phi_* < 0$.

Solution (5.9) clearly shows that the particle apex indeed passes through the plane $\theta = \frac{1}{2}\pi$($\Delta\theta$ changes sign with $(t - t_*)$), due to the non-spheroidal shape of the particle (non-zero m). The passage through the plane of shear $\theta = \frac{1}{2}\pi$ corresponding to (5.9) is illustrated on the plane θ, ψ in figure 12. The passage occurs along the straight lines (in the slice) with the slope

$$\frac{\mathrm{d}\theta}{\mathrm{d}\psi} = -\frac{2\epsilon A_{yx}^2}{\Delta\phi_*}. \tag{5.10}$$

In the case $\psi_* = 0$ or $\pm\frac{1}{2}\pi$ using equations (5.8*a*, *b*) it may be shown that the point $\theta = \frac{1}{2}\pi$, $\psi_* = 0$ is a centre, whereas $\theta = \frac{1}{2}\pi$, $\psi_* = \pm\frac{1}{2}\pi$ are the saddle points. The saddle points play a crucial role in the emergence of the stochastic layer as is shown below.

The results of a numerical solution of the whole system (2.1) or of the reduced system (5.3) for a particle corresponding to the asymptotic limit considered agree with the conclusions of the present asymptotic analysis. In figure 13 the results of the numerical solution of (2.1) corresponding to a very long slender particle with $a_x : a_y : a_z = 100 : 1.1 : 1$ are plotted (in this case $A_{zx} = 1$, $A_{yx} = 1.1$, $\epsilon = 10^{-4}$, $m = [(A_{zx}/A_{yx})^2 - 1]\epsilon^{-1} = -1735.5$, $\epsilon m = -0.1736$). In the phase plane θ, ψ the orbit begins at point A corresponding to the initial conditions and passes through the plane $\theta = \frac{1}{2}\pi$ in figure 13(*a*). The subsequent paths are seen in figure 13(*b*, *c*). In the slice near the plane $\theta = \frac{1}{2}\pi$ the orbits are linear, with a slope depending on the value of $\Delta\phi_*$.

The time series $\theta(t)$, $\psi(t)$ and $\phi(t)$ corresponding to the phase planes of figure 13(*a–c*) are shown in figure 13(*d–f*), respectively. Figure 13(*d*) shows that not every approach to the plane $\theta = \frac{1}{2}\pi$ leads to a passage through it. However after several circuits it happens. The period of tracing of the Jeffery's orbit corresponding to the particle outside the slice is $T = \pi/b = \pi/(\epsilon^{1/2} A_{yx}) = 311$. However, most of the time the particle is aligned in the slice (θ is close to $\frac{1}{2}\pi$, ϕ is close to $\frac{1}{2}\pi + n$) and its motion is governed by (5.8) rather than by (5.4).

A behaviour similar to that shown in figure 13 was found for the same particle subject to different initial conditions.

The resulting Poincaré map depicting the stochastic layer is shown in figure 14.

It is convenient to rearrange the expressions for the Jeffery's orbit (5.4*a*, *b*) into the form

$$\tan\theta = Ca(\sin^2\phi + a^2\cos^2\phi)^{-1/2}. \tag{5.11}$$

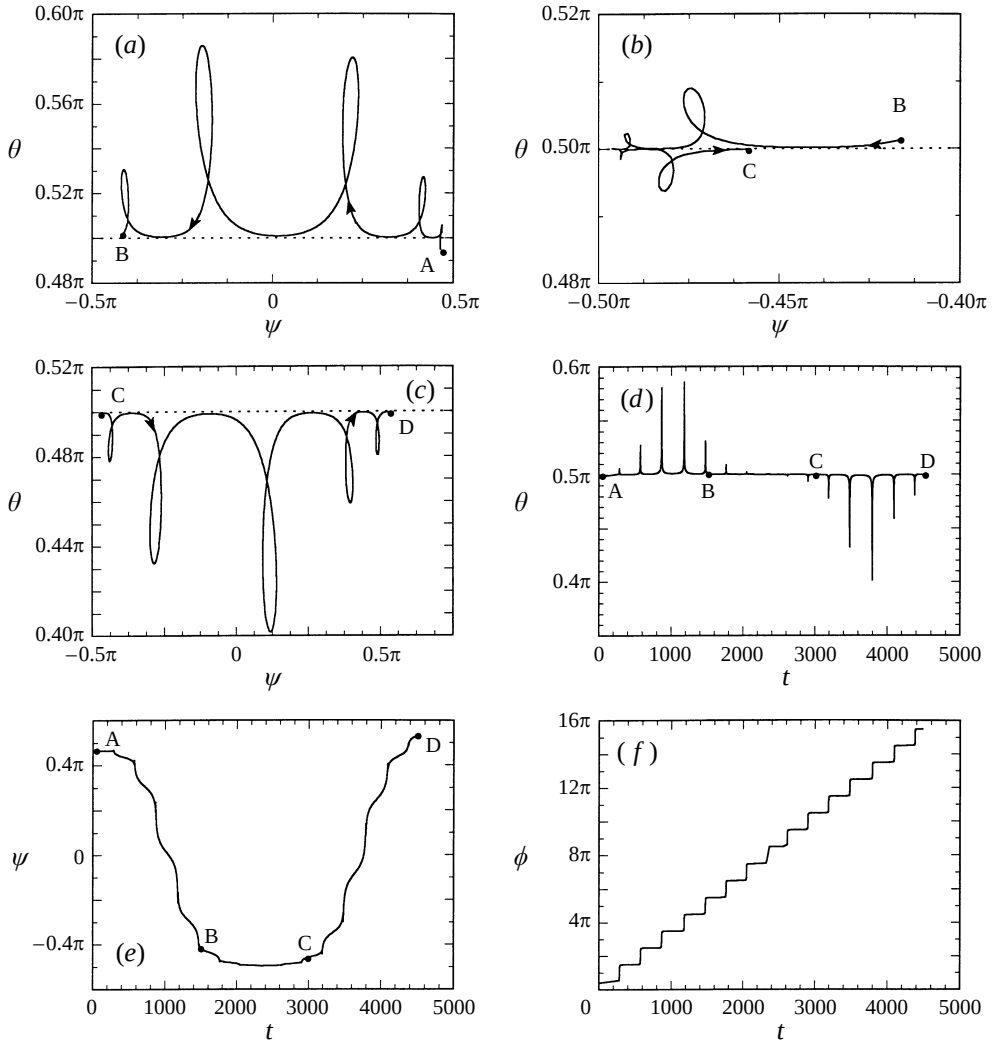

FIGURE 13. A slender nearly axisymmetric particle with $a_x = 100$, $a_y = 1.1$ and $a_z = 1$: (a, b, c) a time sequence of its path in the phase plane θ, ψ; (d, e, f) time series $\theta(t)$, $\psi(t)$ and $\phi(t)$, corresponding to (a), (b) and (c). $\theta_0 = 1.55$, $\psi_0 = 1.55$, $\phi_0 = 0$.

Let the particle apex approach the slice from $\theta < \frac{1}{2}\pi$ along a Jeffery's orbit corresponding to a constant $C = C_-$ in (5.11). The numerical results of figure 13(d) suggest that during the passage of a non-axisymmetric particle through the plane of shear $\theta = \frac{1}{2}\pi$, it slips from a Jeffery's orbit below this plane corresponding to $C = C_- > 0$ to another one with $C = C_+ < 0$, $|C_+| \neq |C_-|$. Note that these orbits are not mirror images of each other relative to the plane $\theta = \frac{1}{2}\pi$. After traversing a new orbit with $C = C_+ < 0$ the particle approaches the slice near $\theta = \frac{1}{2}\pi$ from above and may make a new passage through the plane of shear accompanied by a new slip from the orbit with $C = C_+ < 0$ to another one with $C = C'_- > 0$, $C'_- \neq |C_+|$, and $C'_- \neq C_-$. This process is replicated many times.

Note also that even in the case when the particle apex enters the slice and then leaves it without passing through the plane $\theta = \frac{1}{2}\pi$, the particle slips from one Jeffery's orbit to another one (with orbit constants of the same sign but with different values).

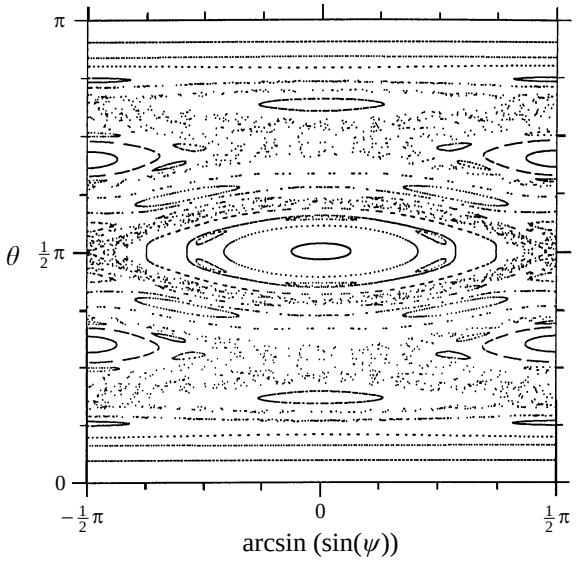

FIGURE 14. The Poincaré map for a particle with $a_x = 100$, $a_y = 1.1$ and $a_z = 1$. Rotation with z parallel to x' ($\theta \equiv \frac{1}{2}\pi$ and $\psi \equiv \frac{1}{2}\pi$) is unstable, whereas rotations with y parallel to x' ($\theta \equiv \frac{1}{2}\pi$ and $\psi \equiv 0$) and x parallel to x' ($\theta \equiv 0$ or π) are stable.

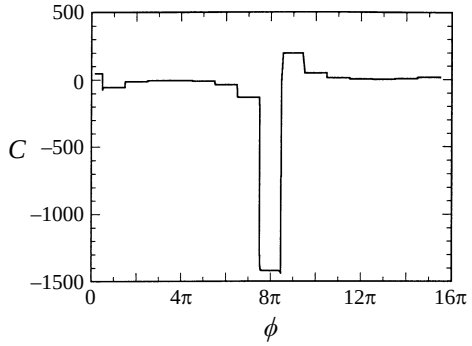

FIGURE 15. Jeffery's orbit constant C for a particle with $a_x = 100$, $a_y = 1.1$ and $a_z = 1$.

The evolution of the orbit constant C calculated from (5.11)

$$C = \frac{\tan\theta}{a}(\sin^2\phi + a^2\cos^2\phi)^{1/2}, \tag{5.12}$$

using $\theta(t)$ and $\phi(t)$ of figure 13(d, f) is shown in figure 15. In this figure, tracing sections of Jeffery's orbits outside the slice corresponds to the sections where C is practically constant whereas ϕ changes (cf. figure 13f where sudden jumps in ϕ correspond to tracing sections of Jeffery's orbits outside the slice). On the other hand, inside the slice the value of C suddenly changes, as is seen in figure 15. Sometimes this leads only to a change in the value of C without a change in its sign (no passage through the plane $\theta = \frac{1}{2}\pi$), whereas for other times both the value and sign of C change (passage through the plane $\theta = \frac{1}{2}\pi$).

The time spent by a particle in the slice (with or without passage through the plane $\theta = \frac{1}{2}\pi$) is incommensurate with the period of Jeffery's orbits $T = \pi/(\epsilon^{1/2}A_{yx})$. The time

intervals between two successive passages through the plane $\theta = \frac{1}{2}\pi$ also become incommensurate with T and with each other. Thus, the instants when passages through the plane $\theta = \frac{1}{2}\pi$ occur are displaced from the instants $bt = \frac{1}{2}\pi + \pi n$ anticipated from the Jeffery's solution to some other instants with non-repeatable intervals between them.

As a result, for some initial conditions chaotic rotation of the particle is observed via a wide-band spectrum resembling that of figure 8(*a*) and a positive Lyapunov exponent. This behaviour was obtained for a 100:1.1:1 particle for several initial conditions leading to the stochastic layer. The motion may be characterized as a slip tunnelling, non-repeatable in time, between two periodic motions corresponding to two families of the Jeffery's orbits below and above the plane $\theta = \frac{1}{2}\pi$. This process leads to the formation of a stochastic layer on the Poincaré maps.

Note also that the numerical simulations of figure 13 are reminiscent of transverse intersections describing the chaotic dynamics of a system where a homoclinic/heteroclinic connection is broken by parametric forcing. However, while the system described by (2.1) or (5.3) consists of a perturbation of a fundamental (Jeffery-like) subsystem and includes a plane of shear ($\theta = \frac{1}{2}\pi$), the latter is not a separatrix in the classic sense of a homoclinic connection to a hyperbolic saddle and a straightforward Melnikov-based analysis cannot be utilized.

Numerical results show that the mechanism leading to the emergence of the stochastic layer is not universal: some quasi-periodic motions can survive, as is seen in figures 6, 11 and 14. Quasi-periodic motions, where slip tunnelling does not lead to a stochastic layer, fill the space around the centre $\theta = \frac{1}{2}\pi$, $\psi = 0$. On the other hand, motions approaching the saddle points $\theta = \frac{1}{2}\pi$, $\psi = \pm\frac{1}{2}\pi$ lead to a stochastic layer as a result of slip tunnelling.

The mechanism leading to a stochastic layer may be elucidated using the following reduced system of equations:

$$\frac{\mathrm{d}\theta}{\mathrm{d}t} = -\tfrac{1}{2}\epsilon^2 A_{yx}^2 m \sin 2\psi, \quad \frac{\mathrm{d}\psi}{\mathrm{d}t} = \tfrac{1}{2}\cos\theta + \tfrac{1}{8}m\epsilon \sin 2\psi \sin 2\phi \qquad (5.13\,a, b)$$

(cf. (5.3*a*, *c*) and (5.8*a*, *c*)), supplemented by (5.4*a*) responsible for the overall variation of ϕ.

The last term on the right in (5.13*b*) includes the coefficient $\sin 2\phi$ which is a periodic function of time. Note that (5.13*a*) does not include Jeffery-like oscillations of θ.

If the last term on the right in (5.13*b*) is cancelled, the system is integrable and the trajectories on the phase plane θ, ψ are given by

$$\sin\theta = \tfrac{1}{2}\epsilon^2 A_{yx}^2 m \cos 2\psi + D, \qquad (5.14)$$

where D is an integration constant.

The family of trajectories (5.14) includes periodic solutions in the form of internal closed loops and external orbits separated by the following heteroclinic connection (see figure 16*a*):

$$\theta = \tfrac{1}{2}\pi \pm \arccos\left[\tfrac{1}{2}\epsilon^2 A_{yx}^2 m(\cos 2\psi + 1) + 1\right]. \qquad (5.15)$$

Near the saddle point $\theta = \frac{1}{2}\pi$, $\psi = \frac{1}{2}\pi$, the heteroclinic connection yields the following limiting lines:

$$\theta = \tfrac{1}{2}\pi \pm (2\epsilon^2 A_{yx}^2 |m|)^{1/2}(\psi - \tfrac{1}{2}\pi). \qquad (5.16)$$

These separatrices are similar to those of the whole system (5.3).

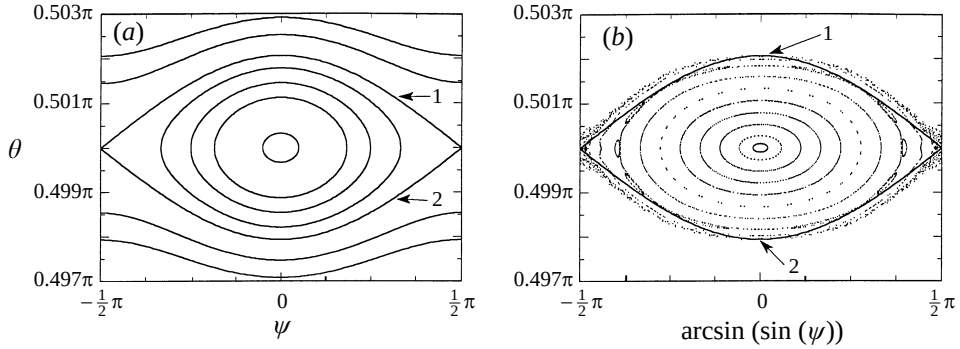

FIGURE 16. (*a*) The phase plane θ, ψ determined by (5.14); (*b*) the Poincaré map obtained via the reduced system (5.13). 1 and 2 show the 'projections' of the separatrices from the phase plane. Particle parameters ϵ, A_{yx} and m correspond to a 100:1.1:1 particle.

However, the last term on the right in (5.13*b*) breaks the separatrices, allowing points close to them to cross from the internal closed loops to the external orbits. The latter may deviate significantly from the closed loops. Such slip through the trajectories may be repeated many times leading to the emergence of a cloud of points near the broken saddle point (figure 16*b*) and its separatrices. Finally the point crosses back over a separatrix and finds itself on a new closed loop which conveys it through the plane $\theta = \frac{1}{2}\pi$. The process will then repeat near the second saddle point $\theta = \frac{1}{2}\pi$, $\psi = -\frac{1}{2}\pi$.

Therefore, we can conclude that a stochastic layer emerges near the broken separatrices of the saddle points. In the cases where sections of the Jeffery's orbits are also involved, they are able to spread chaos away from the slice near $\theta = \frac{1}{2}\pi$ and the saddle points.

6. Conclusions

The rotation of small non-Brownian triaxial ellipsoidal particles immersed in a simple shear flow may become chaotic. The emergence of a stochastic layer was found by means of both numeric and analytic approaches. It results from a broken separatrices of the saddle points, as well as from tunnelling between two periodic motions, non-repeatable in time, corresponding to two families of the Jeffery's orbits below and above the plane $\theta = \frac{1}{2}\pi$. The chaotic rotation manifests itself on the Poincaré map in the form of a stochastic layer which can coexist with quasi-periodic and simple periodic motions.

An immediate consequence of the chaotic motions found in the present work is that an ensemble of random initial orientations of triaxially ellipsoidal particles in dilute suspension does not experience ordering and convergence, and disorder is maintained. However, it seems that this disorder does not make the rheological response of such a system unpredictable and dependent on initial particle orientations. As our computations show, an average shear stress $\tau_{y'z'}$ associated with different initial orientations of a particle, $\tau_{y'z'} \sim \langle \sin^4\theta \sin^2\phi \cos^2\phi \rangle$ (as deduced from the rheological constitutive models for suspensions of rod-like particles; Batchelor 1970 and Rallison & Keiller 1993), takes the same value on different chaotic paths after a short transient.

A. L. Y. would like to thank E. J. Hinch and J. M. Rallison for stimulating discussions. He also acknowledges partial support of this work by EPSRC Research Grant GR/L17092, as well as the hospitality of the Isaac Newton Institute for Mathematical Sciences, University of Cambridge, UK during his visit in April 1996.

Appendix. Numerical integration schemes

The aim of this Appendix is to describe the control of reproduction of the numerical scheme used in the present work to find chaotic solutions leading to formation of a stochastic layer.

Stochastic layers are also found in Hamiltonian systems. It is known that spurious solutions may result from numerical integration of Hamiltonian systems which are simulated without proper adaptive control (Reinhall, Caughey & Storti 1989; Stump 1986; Ablowitz & Herbst 1990). For example, long-time temporal discretization introduces equivalent damping causing orbit deviation, which appears in the system Poincaré map as a stochastic layer. The best way to be confident about Hamiltonian numerics is to use a symplectic integration scheme. If one uses a scheme which does not preserve the canonical solution form (as e.g. Runge–Kutta or Kutta–Merson solvers), one can impose a 'physical' adaptive criterion based on an invariant property of the Hamiltonian system known from the initial conditions.

However, the trace of the Jacobian of the present system (2.1) is shown to be non-zero in §4. This means that the system is non-Hamiltonian, and it does not possess an invariant property that could be used to control the computations. Therefore, the only course of action in our case was the standard numerical check for convergence as we have no invariant property to guide our numerics. We conducted additional simulations with alternative integrations and compared the solutions. The results showed identical periodic and quasi-periodic solutions and marked deviations of chaotic solutions at finite times. The details are given below.

In the present work a Kutta–Merson solver was used to integrate system (2.1). The time step was defined as follows. Let T be a minimum of the periods T_1, T_2 and T_3 given by (2.5d) for the three simple periodic motions corresponding to a given particle. Thus, the time step required for integration was taken as $\Delta t = T/N$ with $N = 50$, 100, 200, 500, etc.

A fourth-order Runge–Kutta solver, with constant time step based on the minimal time step recorded in an initial run obtained from a fifth-order Runge–Kutta scheme, was also compared with the Kutta–Merson solver. For $0 \leqslant t \leqslant 1000$ it yields result identical to that of the Kutta–Merson solver with $N = 500$.

Also a fourth-order Rosenbrock solver for integrating stiff ordinary differential equations, with monitoring of local truncation error to adjust stepsize, was compared with the Kutta–Merson and Runge–Kutta solvers. For the same test case, its results deviated from the previous ones at about $t = 300$. We also tested a Bulirsch and Stoer solver for stiff ordinary differential equations, verifying the above results.

Thus for $0 \leqslant t \leqslant 1000$ the most reliable results (certainly including early time details of the Poincaré maps) were obtained with the Kutta–Merson solver with $N = 500$, and it was used in further computations. This solver was also found to be time-reversal symmetric at $0 \leqslant t \leqslant 1000$.

It is emphasized that it is impossible to obtain identical results for much longer time runs by further increasing N and decreasing time step, which shows that chaotic motions are, in principle, uncomputable.

Note also that reproduction of the results corresponding to the periodic or quasi-periodic motions obtained with different values of N is much better.

REFERENCES

Ablowitz, M. J. & Herbst, B. M. 1990 On homoclinic structure and numerically induced chaos for the nonlinear Schrodinger equation. *SIAM J. Appl. Maths* **50**, 339–351.

Batchelor, G. K. 1970 The stress system in a suspension of force-free particles. *J. Fluid Mech.* **41**, 545–570.

Gierszewski, P. J. & Chaffey, C. E. 1978 Rotation of an isolated triaxial ellipsoid suspended in slow viscous flow. *Can. J. Phys.* **56**, 6–11.

Hinch, E. J. & Leal, L. G. 1979 Rotation of small non-axisymmetric particles in a simple shear flow. *J. Fluid Mech.* **92**, 591–608.

Jeffery, G. B. 1922 The motion of ellipsoidal particles immersed in a viscous fluid. *Proc. R. Soc. Lond.* A **102**, 161–179.

Joseph, D. D. 1976 *Stability of Fluid Motions*. Springer.

Lichtenberg, A. J. & Lieberman, M. A. 1992 *Regular and Chaotic Dynamics*. Springer.

Rallison, J. M. & Keiller, R. A. 1993 Sink flows of a suspension of rigid rods. *J. Non-Newtonian Fluid Mech.* **48**, 237–259.

Reinhall, P. J., Caughey, T. K. & Storti, D. W. 1989 Order and chaos in a discrete Duffing oscillator – indications on numerical integration. *Trans. ASME*: *J. Appl. Mech.* **52**, 162–167.

Stump, D. R. 1986 Solving classical mechanics problems by numerical integration of Hamilton's equations. *Am. J. Phys.* **54**, 1096–1100.

Szeri, A. J. 1993 Pattern formation in recirculating flows of suspensions of orientable particles. *Phil. Trans. R. Soc. Lond.* A **345**, 477–506.

Szeri, A. J. & Leal, L. G. 1993 Microstructure suspended in three-dimensional flows. *J. Fluid Mech.* **250**, 143–167.

Szeri, A. J., Milliken, W. J. & Leal, L. G. 1992 Rigid particles suspended in time-dependent flows: irregular versus regular motion, disorder versus order. *J. Fluid Mech.* **237**, 33–56.